Showcasing research from Professor Weijie Li's laboratory, State Key Laboratory for Powder Metallurgy, Central South University, Changsha, China.

An electron-losing regulation strategy for stripping modulation towards a highly reversible Zn anode

Aqueous zinc-ion batteries have attracted widespread attention as candidates for next-generation energy storage systems. Uneven plating/stripping of zinc can cause irreversible electrodes during cycling. In this work, an electro-losing regulation strategy for stripping modulation by adding Oxolane additives is proposed. According to experimental results, this study provides new guidance for the design of electrolyte additives.

ROYAL SOCIETY
OF **CHEMISTRY**

rsc.li/chemical-science

An electron-losing regulation strategy for stripping modulation towards a highly reversible Zn anode†

Xinyi Wang,‡[ab] Liyang Liu, [iD] ‡[a] Zewei Hu,[a] Chao Han,[c] Xun Xu,[b] Shixue Dou [iD] [bd] and Weijie Li [iD] *[ab]

The practical application of aqueous zinc-ion batteries (AZIBs) is hindered by their low coulombic efficiency (CE) and unstable cycle life. Numerous electrolyte-additive-related studies have been performed, but most of the focus has been on the Zn plating process. In fact, practical AZIBs undergo stripping in practice rather than plating in the initial cycle, because the commonly used cathodes in the charged state do not have zinc ions, so a uniform stripping process is crucial for the cell performance of AZIBs. Here, we propose an electron-losing regulation strategy for stripping modulation by adding additives. Oxolane (OL) was chosen as the model additive to verify this assumption. It is found that OL adsorbs onto the uneven initial Zn surface and accelerates the dissolution of the Zn tips, thus providing a uniform Zn anode during the stripping process. The oxygen atoms in OL reduce the surface energy of Zn and promote the exposure of the Zn (002) surface during plating. Consequently, cells with the OL electrolyte additive maintained a long lifespan and showed superior reversibility with a high average CE. The findings of this work lead to a deep understanding of the underlying mechanism of Zn anode stripping and provide new guidance for designing electrolyte additives.

Introduction

Electrochemical energy storage, possessing the advantages of convenience and eco-friendliness, has been widely studied to make the best of green and clean energy.[1,2] Due to their intrinsic characteristics of low cost, high theoretical capacity (820 mA h g^{-1}), and safety, aqueous zinc ion batteries (AZIBs) have attracted widespread attention as a great potential candidate for next-generation energy storage systems.[3–9] Nevertheless, there are still some issues relating to the Zn anode, including side reactions (corrosion and hydrogen evolution reactions) and Zn dendrite growth, causing low coulombic efficiency and unstable cycle life and consequently hindering the commercialization of AZIBs. The complex interfacial reactions on the Zn surface and uneven Zn deposition will lead to the growth of Zn dendrites. The continuously protruding dendrites will shed and even pierce the separator, which can finally lead to the deterioration of the cycling stability of the battery.[10–13] Therefore, the related research on interface engineering of Zn anodes has taken center stage.

To solve the problems of the Zn anode interface, the current strategies can be summarized into three aspects: artificial interface-layer construction,[14–16] electrolyte optimization,[17–21] and current collector modification.[22–24] Among them, the electrolyte optimization is the most straightforward strategy with excellent reproducibility.[5,25] This is because it does not involve complicated processes, and only a tiny amount of additive can significantly improve the properties of the electrolyte. In general, electrolyte additives play the following roles in adjusting the Zn anode interface: (1) weakening the solvation interaction of Zn^{2+} with H$_2$O to decrease water activity, thus reducing side reactions such as the hydrogen evolution reaction on the anode side;[26] (2) providing a shielding effect by preferential adsorption of exotic cations on the initial Zn tips, preventing further Zn^{2+} deposition in the tip area to suppress the dendrite growth;[27,28] (3) potentially guiding the oriented growth of the Zn close-packed plane to expose Zn (002) instead of Zn (101) and Zn (100), which favors reversible Zn stripping/plating;[29,30] (4) assisting the formation of a solid-electrolyte interphase (SEI) on the Zn anode through the decomposition of electrolyte components, which presents more capacity for self-repair than artificial SEI coating layers.[31,32] To date, numerous additive-related studies have been dedicated to solving the issues of the Zn anode by the above approaches, but most focus has been

State Key Laboratory for Powder Metallurgy, Central South University, Changsha, 410083, China. E-mail: li-306@csu.edu.cn

Institute for Superconducting and Electronic Materials, Australian Institute for Innovative Materials, University of Wollongong, Wollongong, 2522, Australia

School of Materials Science and Engineering, Central South University, Changsha, 410083, China

Institute of Energy Materials Science, University of Shanghai for Science and Technology, Shanghai, 200093, China

† Electronic supplementary information (ESI) available. See DOI: https://doi.org/10.1039/d4sc04611k

‡ These authors contributed equally to this work.

directed towards the Zn plating process. The Zn stripping process, however, has generally been disregarded.

The storage mechanism of the Zn anode for AZIBs is the process for the plating/stripping of Zn^{2+} ions.[33] Thus, uneven plating/stripping can cause irreversible changes to the electrodes during cycling.[34,35] Actually, in the initial cycle, AZIBs undergo stripping rather than plating, because the commonly used cathodes have no zinc ions in the charged state (e.g., V_2O_5 and MnO_2). Pits will first form on the Zn surface during the stripping process, due to the nonuniform metal dissolution. Then, the pits are filled with mossy deposited Zn during the subsequent plating process. After a few cycles, some of the mossy Zn evolves into "dead Zn", significantly reducing the reversibility of the Zn anode.[36] Therefore, it can be seen that a uniform stripping process is crucial for the cell performance of AZIBs. The stripping is a process of metal dissolution where the Zn metal loses electrons and transforms into Zn^{2+}. This means that regulating the ability of Zn to lose electrons can influence the Zn stripping process. Therefore, we propose an electron-losing regulation strategy for stripping modulation by introducing electrolyte additives. These additives need to be able to preferentially adsorb onto the surface of the zinc anode. Additionally, they should contain highly electronegative atoms such as O (3.44), F (3.98), and S (2.58), which have high electron-attracting capability, thereby possibly enhancing Zn dissolution. Moreover, it is better to choose small organic molecules as the additives to mitigate the deterioration of the deposition kinetics caused by the steric hindrance of macromolecules.[37] Oxolane (OL, C_4H_8O) is a small-organic-molecule solvent that contains electronegative oxygen atoms and is readily miscible with H_2O. In addition, as a cyclic ether, the oxygen atoms in OL can form hydrogen bonds with H_2O, thereby reducing water activity and consequently reducing the side reactions of Zn.[38] Until now, there has been no report or study on whether OL could regulate the stripping process of Zn anodes. Thus, it is worth investigating whether OL can act as a bifunctional additive to simultaneously modulate the Zn plating/stripping process and to determine the underlying mechanism.

Herein, we have chosen OL as our model additive to verify the assumption of its value for an additive-modulating stripping strategy. Through simulation and calculations, we have found that the work function of Zn significantly decreases from 3.67 eV to 3.08 eV after adsorbing OL, as shown in Fig. 1a. The work function represents the minimum energy required for electrons to escape from the interior of the metal.[39] The smaller the work function, the easier it is for electrons to leave the metal. The differential charge density also shows electron cloud transfer from the Zn surface to OL (Fig. 1b and c). This indicates that OL can facilitate the loss of electrons from Zn metal to transform it into Zn^{2+}, thereby demonstrating that OL possesses the ability to regulate the Zn stripping process. During Zn stripping, OL adsorbs on and is concentrated at the tips of the Zn surface, boosting the dissolving speed of the initial protuberant tips and consequently leading to uniform stripping. As for plating, experimental characterization and theoretical simulations confirmed that OL molecules induce the (002) orientation for Zn deposition and thus inhibit the dendrite growth. Thus, the modified electrolyte exhibits excellent electrochemical performance. Zn‖Zn cells with 2 m $Zn(OTF)_2$/OL maintained a long lifespan of more than 3200 h, and Zn‖Cu cells showed stability and reversibility for up to 1400 cycles with an average coulombic efficiency (CE) of 99.3% due to the strong
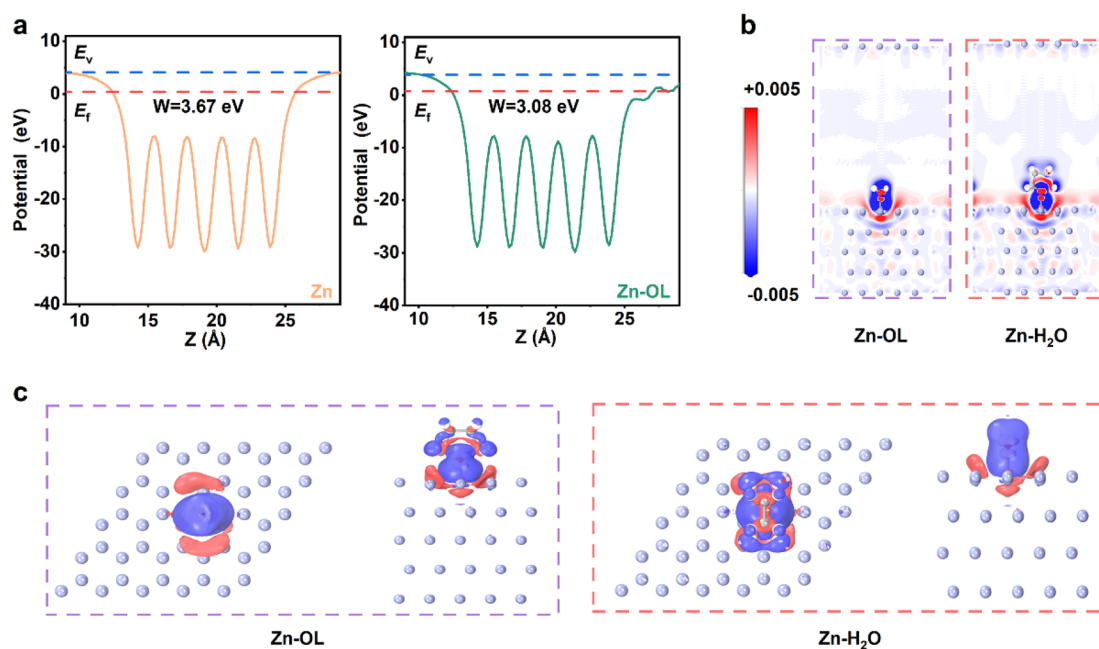

Fig. 1   Simulation of the effect of the OL additive: (a) the work function of Zn (002) with and without OL. (b) Charge density difference between OL and H_2O on Zn (002). The red color means electron accumulation and the blue means electron deficiency. (c) Top view and side view 3D images of the charge density differences between OL and H_2O on Zn (002).

inhibition of dendrite growth and by-products. In addition, a full cell with a NaV$_3$O$_8$·1.5 H$_2$O (NVO) cathode and a commercial Zn metal anode exhibited excellent cycling performance for more than 3000 cycles. This work not only provides a new strategy of stripping modulation to improve the electrochemical performance of AZIBs, but also provides novel and comprehensive insight into the impact and mechanism of this electrolyte additive on uniform Zn stripping/plating.

Results and discussion

Verification of the electron-losing regulation strategy for stripping modulation

To verify the assumptions of the electron-losing regulation strategy, density functional theory (DFT) calculations were carried out to evaluate the ability of OL to adsorb on the Zn anode and the electron-losing capability of the Zn anode after the adsorption of OL. As shown in Fig. 2a, the adsorption energy
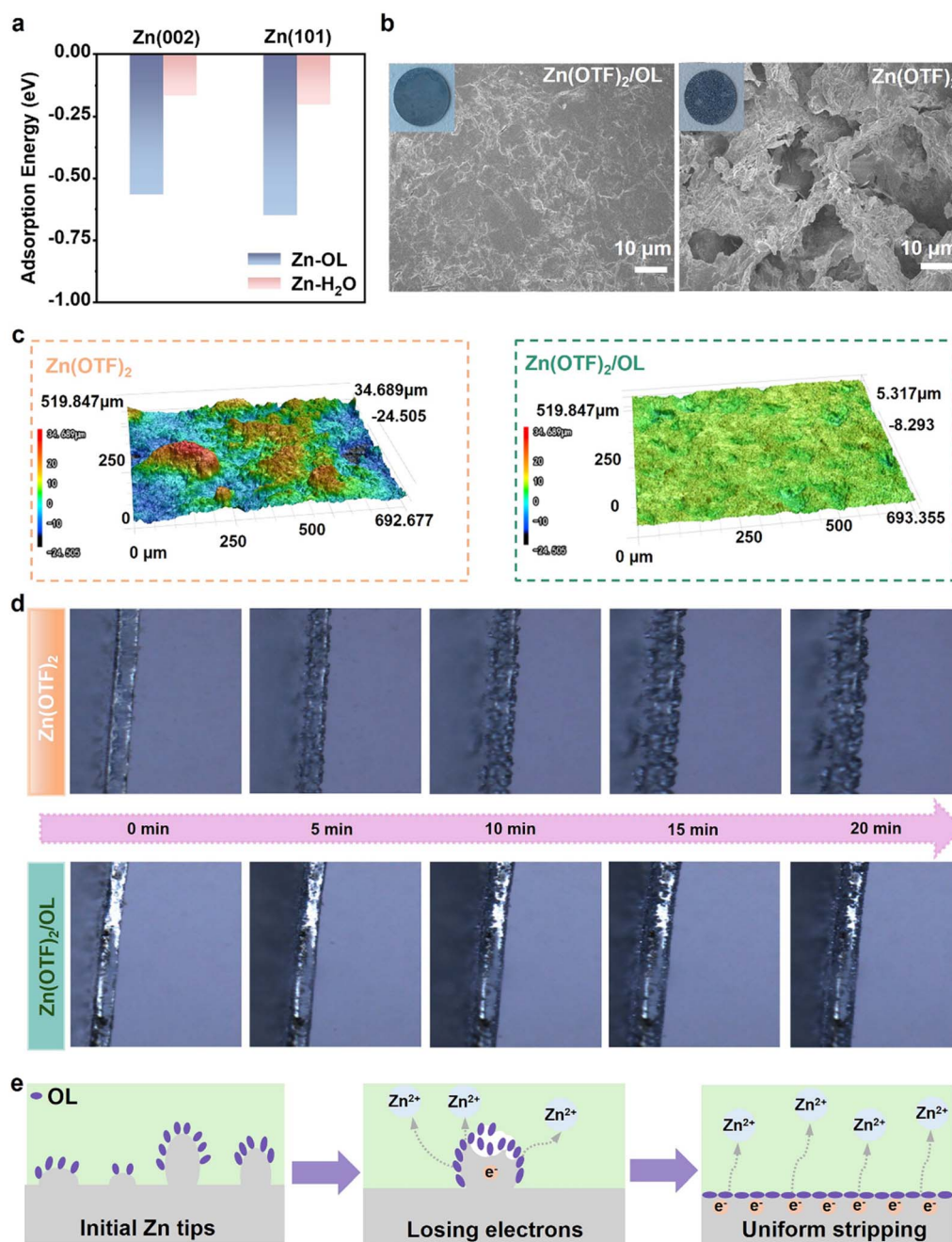

Fig. 2 Evaluation of OL modulation of the Zn stripping. (a) Adsorption energies of H$_2$O and OL molecules on the Zn anode. (b) SEM images and digital images of anodes after stripping for 20 h in different electrolytes. (c) 3D reconstructions of SLCM images of Zn electrodes. (d) *In situ* optical microscope images of the Zn stripping process in Zn(OTF)$_2$ and Zn(OTF)$_2$/OL electrolytes. (e) Schematic illustration of the mechanism of OL that facilitates the loss of electrons from the initial Zn tips.

of OL is much lower than that of H_2O on the Zn anode. Especially on the Zn (002) surface, the adsorption energy of OL and H_2O is −0.57 and −0.16 eV, respectively. The adsorption energy of OL on the Zn surface is more negative. This demonstrates that OL can adsorb on the Zn surface more effortlessly than H_2O. The adsorption energy of OL and H_2O on the Zn (101) surface is −0.65 and −0.20 eV, respectively, which shows the same trend as that on the Zn (002) surface, demonstrating that OL tends to replace H_2O to adsorb on the Zn surface. In addition, the work function (Fig. S1, ESI†) and the differential charge density results (Fig. S2, ESI†) for Zn (101) with or without adsorbed OL confirm that OL can facilitate the loss of electrons from Zn metal to transform it into Zn^{2+}, thereby demonstrating that OL possesses the ability to regulate the Zn stripping process. When the Zn anode is immersed in OL, the OL tends to adsorb around Zn tips, which can accelerate their dissolution. As a result, Zn tips have a greater propensity to lose electrons and transform into Zn^{2+}, consequently presenting a uniform stripping process.

To further understand the effect of OL on the stripping of the Zn anode, the electrodes after stripping were characterized by scanning electron microscopy (SEM). To more clearly observe the morphological evolution of Zn during the stripping process, the Zn electrodes were stripped for longer times (10 h and 20 h) than in normal testing. SEM images and digital photographs of the anodes after stripping for 10 h and 20 h in $Zn(OTF)_2$ and $Zn(OTF)_2/OL$ (with 7.5 vol% OL chosen as the representative electrolyte) aqueous electrolytes are shown in Fig. S3 (ESI)† and Fig. 2b, respectively. In the modified electrolyte, a smooth Zn surface can be observed (Fig. 2b). In contrast, the Zn surface presents a porous morphology after stripping in the $Zn(OTF)_2$ electrolyte, demonstrating that the anode surface is severely corroded. This indicates that, without OL, the dissolution sites of the Zn anode are not uniform. This further demonstrates the capacity of OL to regulate uniform Zn stripping on the Zn surface.

To further verify that the OL additive promotes uniform Zn stripping, scanning laser confocal microscopy (SLCM) measurements were conducted to observe the three-dimensional (3D) morphology of cycled Zn anodes after discharging. As shown in Fig. 2c, a large number of cavities appear on the Zn surface after stripping in the baseline electrolyte with isolated dendrites having lengths of ∼34.689 μm, which indicates that the dissolution process of the Zn anode is nonuniform in the $Zn(OTF)_2$ electrolyte. In contrast, the Zn anode after discharging in the electrolyte with OL addition presented a relatively flat surface without obvious protrusions and cavities. The altitude intercept is only ∼5.317 μm. Line roughness measurement based on the 3D reconstructions of SLCM images of Zn electrodes was also provided to prove that OL produces more uniform Zn electrodes (Fig. S4, ESI†). Under OL treatment, the line roughness of the electrode closely matches the baseline. In contrast, the electrode without OL exhibits a significantly rougher surface compared to the baseline. Digital images from side and top views of 2D versions of electrodes also show the same trend (Fig. S5 and S6, ESI†). This also proves that OL has the function of regulating Zn stripping behavior. The Zn

stripping behavior in the $Zn(OTF)_2$ and $Zn(OTF)_2/OL$ electrolytes was further tested by *in-situ* optical microscopy system (Fig. 2d). In the bare $Zn(OTF)_2$ electrolyte, an uneven dissolution phenomenon was observed on the Zn anode surface after just 5 min of stripping, and it became more serious during the continuous stripping. In contrast, the Zn foil exhibited uniform dissolution behavior in electrolytes containing OL. The stripping process appeared uniform and stable.

Fig. 2e illustrates the details of the mechanism of OL to promote the dissolution of Zn. Based on experimental and theoretical analysis, it can be concluded that OL preferentially adsorbs and accumulates at the convex tips of the initial zinc foil rather than on other flatter surfaces during stripping. Similar to the tip effect, more OL additives tend to accumulate at the protrusions of the initially uneven zinc foil surface. Compared to a flat zinc surface, electrons tend to concentrate at the tips. Owing to the electronegative oxygen atoms contained in OL, OL could adjust the ability of losing electrons from Zn atoms, accelerating the Zn dissolution from the tip until the tip completely disappears on the Zn surface. Finally, OL is adsorbed on the already flat surface of Zn, inducing uniform dissolution of Zn.

Evaluating the effects of OL on the solvation structure and SEI film

To explore how OL practically affects the solvation structure, Fourier transform infrared spectroscopy (FTIR), Raman spectroscopy, and nuclear magnetic resonance (NMR) of the 2 m $Zn(OTF)_2$ aqueous electrolytes with different volume ratios of OL (denoted as OL x, $x = 0$, 5, 7.5, 10, 20, 30, and 40 vol%) were performed. As shown in Fig. 3a and S7 (ESI),† with increasing OL volumes, a blue shift of the peak positions for O–H (H_2O) stretching (3000–3500 cm^{-1}) and H–O (H_2O) bending (1600–1700 cm^{-1}) appears, which indicates the increasing strength of O–H in the H_2O molecule. This is because the interaction between H_2O and OL disturbs the original hydrogen-bond network of H_2O.[40] Specifically, OL molecules form a hydrogen connection with H_2O molecules, thereby weakening the hydrogen bonds between H_2O molecules, which reduces their activity.

The results from Raman spectra and NMR spectra also prove the interactions generated between OL and H_2O. The Raman spectra of the electrolytes (Fig. 3b) show that the C–H stretching of OL at ∼2952 cm^{-1} moves to a lower wavenumber (∼2853 cm^{-1}) as the amount of OL increases, which signifies that OL interacts with Zn^{2+} and H_2O. In addition, the peak between 3000 and 3750 cm^{-1}, which can be attributed to O–H (H_2O) stretching, exhibits a blue shift with the gradual addition of OL. This is consistent with the results from the FTIR spectra, further demonstrating a decrease in the strength of hydrogen bonds involving H_2O. The ^1H NMR spectra of the electrolytes are shown in Fig. S8 (ESI).† The peak at 4.79 ppm is the ^1H resonance of H_2O. An obvious shift to a higher field occurs from 4.64 ppm to 4.81 ppm after increasing the concentration of OL. These shifts indicate a decrease in the electron density of ^1H (H_2O), demonstrating that OL interacts strongly with H_2O
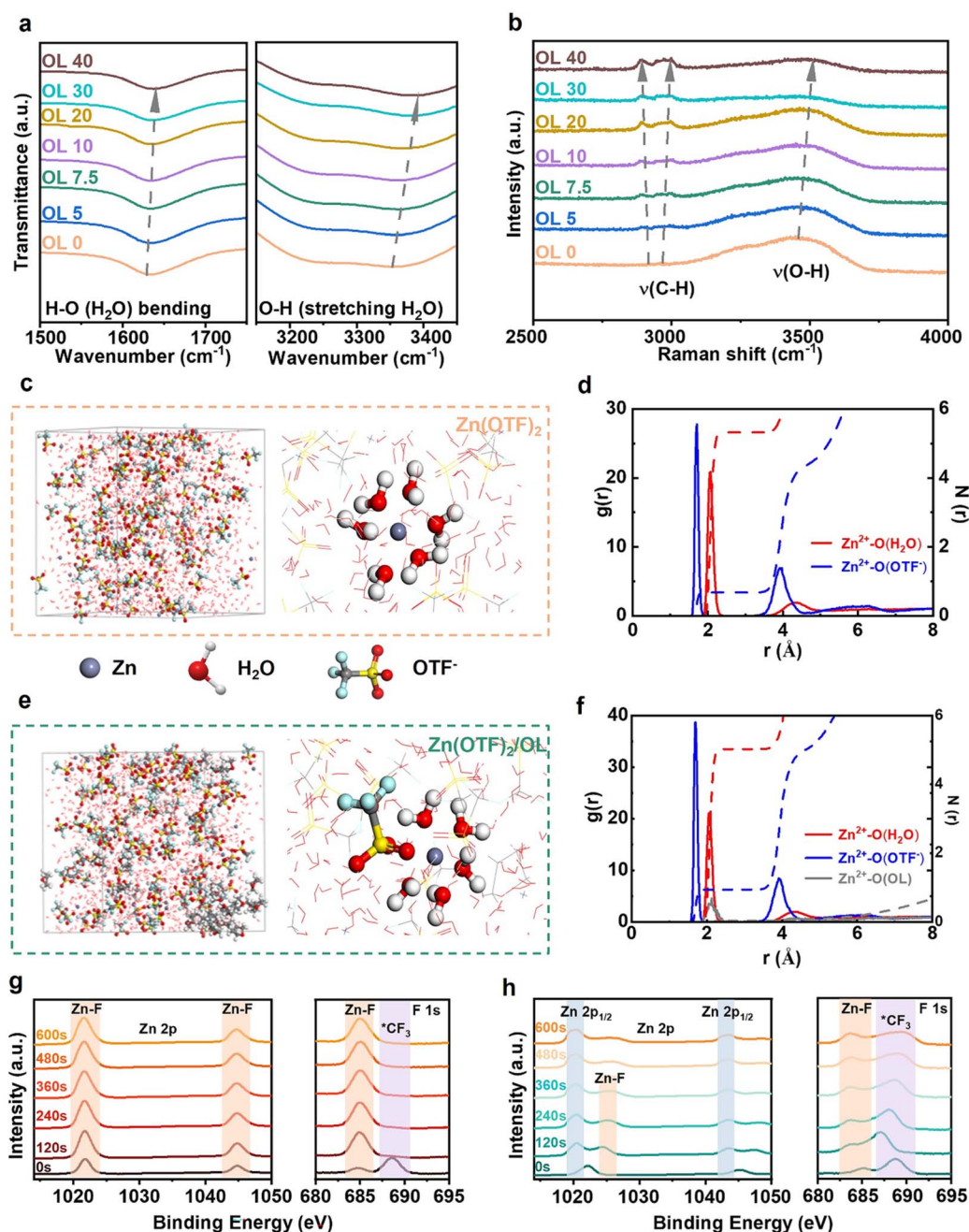
Fig. 3 Characterization of electrolytes and SEI films. (a) FTIR spectra and (b) Raman spectra of the OL 0, OL 5, OL 7.5, OL 10, OL 20, OL 30 and OL 40 electrolytes. Simulation of (c) $Zn(OTF)_2$ and (e) $Zn(OTF)_2/OL$ electrolytes. RDF plots of (d) $Zn(OTF)_2/OL$ and (f) $Zn(OTF)_2/OL$. Depth profiling XPS spectra (Zn 2p, F 1s, and C 1s) of the SEI layer on electrodes in (g) $Zn(OTF)_2$ and (h) $Zn(OTF)_2/OL$ electrolytes after 20 cycles.

through hydrogen bonding. These spectral results demonstrate that the OL additive can reduce the activity of H_2O by weakening the hydrogen bonds between them. By measuring the ionic conductivity of these electrolytes, it is evident that the $Zn(OTF)_2$ electrolyte exhibits the highest ionic conductivity (66.83 mS cm^{-1}), and the ionic conductivity decreases with increasing OL volumes (Fig. S9, ESI†). The change in ionic conductivity is due to the change in the coordination environment of the electrolyte caused by the addition of the OL additive. Ionic conductivity is critical for the low-temperature performance of

electrochemical energy storage devices. Testing the ionic conductivity of electrolytes with varying volume of OL at temperatures of 15 °C, 7.5 °C, 0 °C, and −2.5 °C reveals that ionic conductivity decreases as the temperature drops (Fig. S10, ESI†). To further investigate the impact of OL additives on the electrolyte at low temperatures, differential scanning calorimetry (DSC) tests were conducted (Fig. S11, ESI†). The results indicated that the electrolyte crystallized at −53 °C without OL additive, while the presence of OL additive caused crystallization at −62 °C. This is because OL disrupts the original

hydrogen bond network between water molecules, lowering the freezing point of electrolytes. The interaction between the organic solvent and water molecules prevents the formation of a structured hydrogen bond network. Although this approach effectively reduces the freezing point of aqueous electrolytes, it also introduces significant drawbacks. The addition of organic solvents reduces the ionic conductivity, leading to decreased performance of the ZIBs.

To further explore the Zn^{2+}-solvation structure, molecular dynamics (MD) simulations were then performed in different electrolytes. In $Zn(OTF)_2$ (Fig. 3c), Zn^{2+} is coordinated with six H_2O molecules in the first solvation shell, as expected, and the contribution from OTF^- is negligible. In contrast, a different solvation structure can be observed when OL is added. It is shown that OTF^- is involved in the solvation shell of Zn^{2+} in $Zn(OTF)_2$/OL (Fig. 3e). Radial distribution functions (RDFs) determine the distributions of surrounding molecules to elucidate the electrolyte environment.[41] The corresponding RDFs of $Zn(OTF)_2$ and $Zn(OTF)_2$/OL were then calculated (Fig. 3d and f). The plot for the $Zn(OTF)_2$ electrolyte shows a sharp Zn^{2+}-O (H_2O) peak at ~2.07 Å, which reveals the arrangement of H_2O around Zn^{2+}. In the curve of $Zn(OTF)_2$/OL, however, a new peak related to Zn^{2+}-O (OL) appears at the same peak position of Zn^{2+}-O (H_2O), which indicates that OL changes the primary solvation sheath of Zn^{2+}. When 40 vol% OL was added, the OL molecules showed a greater tendency to aggregate, and more OTF^- was involved in the solvation shell of Zn^{2+} (Fig. S12, ESI†), which again indicates that OL is involved in the Zn^{2+} solvation structure. These results again demonstrated that OL is beneficial for the emergence of Zn^{2+}-OTF^- contact ion couples and aggregates.

The formation of SEI layers on the Zn electrodes cycled in $Zn(OTF)_2$ and $Zn(OTF)_2$/OL was verified by X-ray photoelectron spectroscopy (XPS) using depth profiling with Ar^+-ion etching sources. The F 1s and Zn 2p spectra of the Zn anode from $Zn(OTF)_2$ are shown in Fig. 3g. Although the *CF_3 organic fluorine peak at 689.5 eV is detectable, the internal component of the SEI layer does not present *CF_3 anymore.[42] Even after Ar^+ sputtering for 600 s, the Zn–F signal remains detectable and robust, indicating that the ZnF_2 layer formed in the $Zn(OTF)_2$ electrolyte was very loose and ineffective in inhibiting Zn dendrite growth. In contrast, the SEI formed in the $Zn(OTF)_2$/OL electrolyte was analyzed after different sputtering times (Fig. 3h). The Zn metal signal gradually increases as the sputtering time is prolonged and becomes dominant. This indicates that the ZnF_2 layer is thin. In addition, the C element from the organic components was characterized (Fig. S13, ESI†). The peaks for C–C and C–H detected on the Zn anode from $Zn(OTF)_2$ gradually decreased with time during the etching process. In sharp contrast, these peaks were only detected on the Zn anode taken from the $Zn(OTF)_2$/OL electrolyte in the initial state. Moreover, according to the atomic concentration of the SEI component of the anode taken from the $Zn(OTF)_2$/OL electrolyte (Fig. S14, ESI†), the content of C is significantly reduced, which proves that the content of organic carbon in the SEI is relatively low. These results indicate that, in the $Zn(OTF)_2$/OL electrolyte,

a dense and thin SEI layer is formed on the Zn anode during the plating process.

Texture formation of Zn during the plating process

Zn plating behavior with different electrolytes was then investigated. Fig. 4a shows the X-ray diffraction (XRD) patterns of the Zn electrode after plating for 20 h in $Zn(OTF)_2$/OL and $Zn(OTF)_2$. Notably, several new peaks are evidenced in the curve of the Zn anode taken from $Zn(OTF)_2$ and are similar to those in previous studies and represent the typical by-product peaks of $Zn_x(OTF)_y(OH)_{2x-y} \cdot nH_2O$.[43,44] Clearly, this indicates that a more serious corrosion reaction occurred on the Zn anode with $Zn(OTF)_2$. In contrast, the XRD peaks of the Zn cycled in the $Zn(OTF)_2$/OL electrolyte remained the same as those of pristine Zn, demonstrating the anticorrosion properties of the OL additive.

The intensity of the (002) peak also becomes stronger for the Zn electrode cycled in the modified electrolyte. The peak intensity ratio of $I_{(002)}/I_{(101)}$ increases greatly for the Zn anode cycled in the $Zn(OTF)_2$/OL electrolyte ($I_{(002)}$: $I_{(101)} = 0.373$), compared with the pristine Zn anode ($I_{(002)}$: $I_{(101)} = 0.142$) and that cycled in the $Zn(OTF)_2$ electrolyte ($I_{(002)}$: $I_{(101)} = 0.101$). The (002) texture is confirmed to be beneficial for even Zn deposition.[18] Specifically, the hexagonal close-packed (hcp) arrangement of the (002) crystal plane has the lowest surface energy in Zn metal and has a smoother and more uniform interface charge density than the (100) crystal plane.[45] This lowest surface energy makes the (002) plane less electrochemically active.[46] Therefore, surfaces with more exposed (002) planes may slow down corrosion and hydrogen evolution while mitigating the generation of by-products.

The *in-situ* XRD pattern more intuitively shows the dynamic changes of the (002) and (101) crystal planes during the discharge process (Fig. 4b and S15, ESI†). In the early stage of discharge, the signal of Zn (002) is weak. As the reaction time increases, more and more Zn is deposited during the plating process, and the signal of Zn (002) is significantly enhanced. The final exposure of the Zn (002) plane means that OL modulates the Zn plating behavior. Fig. 4c shows the surface energy of different Zn planes in the electrolyte with and without OL and their corresponding adsorption models. Crystals typically grow by steadily decreasing their total surface energy.[47] When oxygen atoms from OL are adsorbed on the Zn surface, Zn (002) has the smallest surface energy. The surface energy decreases from 2.01 J m^{-2} to 1.93 J m^{-2}. The decreased surface energy of Zn (002) means that the nucleation resistance of Zn (002) is further reduced, so preferential orientation of Zn electrodeposition along (002) is achievable.

The morphology of the electrodes after 20 cycles in OL electrolyte also shows the final exposure of the Zn (002) plane (Fig. 4d). The electrode cycled in the $Zn(OTF)_2$ electrolyte showed a loose deposited Zn morphology, which could easily fall off and form "dead" Zn, finally causing a short circuit. In contrast, the electrode deposited in the electrolyte containing OL for 20 cycles showed a tight and dense surface. In the higher magnification SEM image, regular and parallel hexagonal Zn
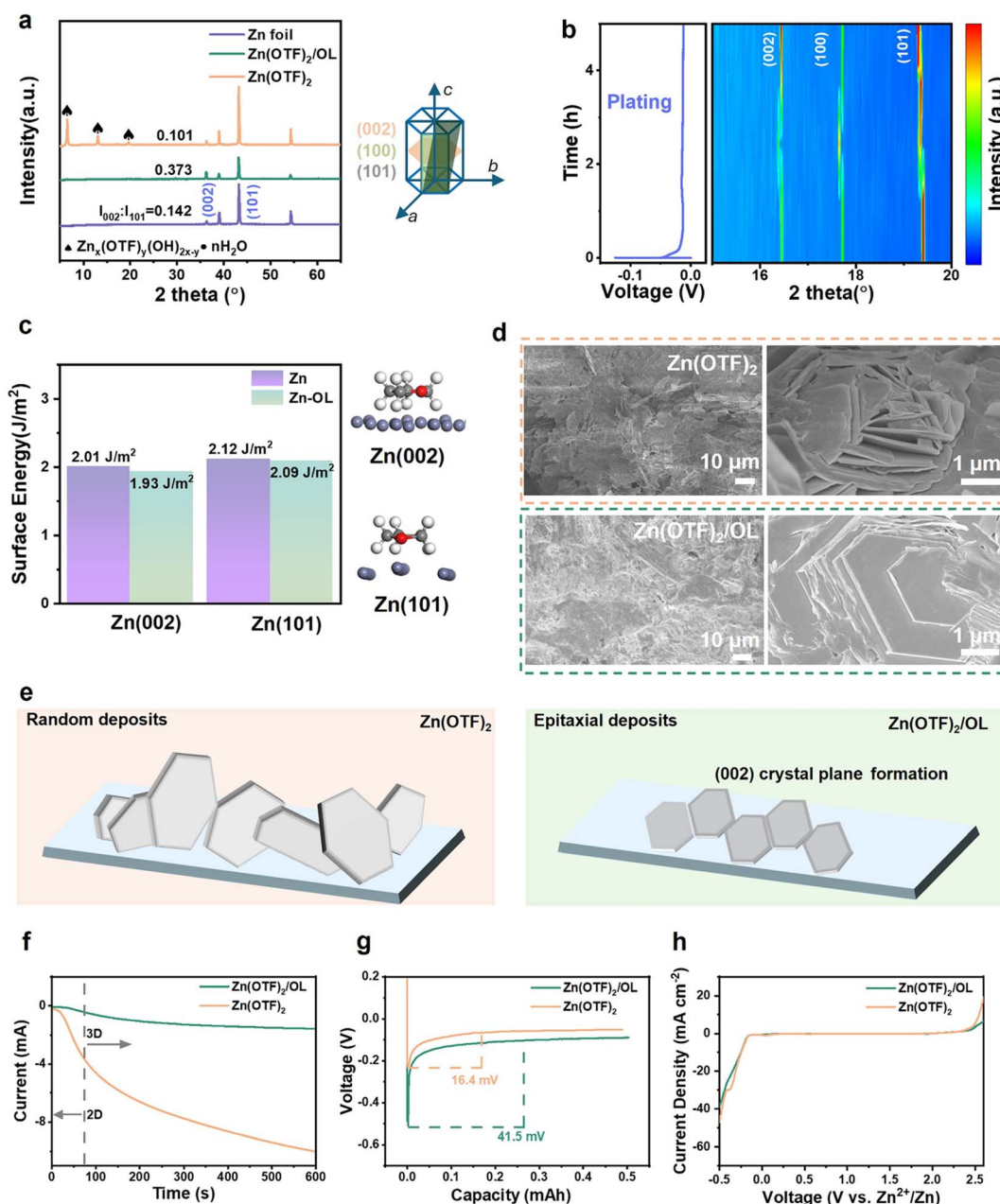
Fig. 4 Characterization of the Zn electrodes *via* the OL regulating plating process. (a) XRD patterns of Zn‖Zn cells in $Zn(OTF)_2$/OL and $Zn(OTF)_2$ after discharge for 20 h at 1 mA cm^{-2} and 1 mA h cm^{-2}. (b) *In situ* XRD patterns of Zn plating deposited for 5 h. (c) Surface energy of Zn foil and after OL adsorption. (d) Zn electrodes after 20 cycles at 1 mA cm^{-2} and 1 mA h cm^{-2} in different electrolytes. (e) Schematic illustrations of the Zn plating mechanism on different planes. (f) CA of Zn‖Zn symmetric cells. (g) Initial Zn nucleation overpotential of Zn‖Cu cells at 1 mA cm^{-2}. (h) LSV characterization in different electrolytes.

plates appear in the $Zn(OTF)_2$/OL electrolyte, which corresponds to the gradually increasing Zn (002) peak in the XRD results. The morphologies and cross-sectional view of Zn electrodes from $Zn(OTF)_2$/OL and $Zn(OTF)_2$ after 50 cycles are shown in Fig. S16 (ESI).† The Zn electrode in $Zn(OTF)_2$ shows mossy growth after 50 cycles, and the cross-section of the 70 μm thick plated Zn also evidences extensive by-products and inhomogeneous Zn deposition. In contrast, the Zn anode from $Zn(OTF)_2$/OL maintains a flat and smooth surface, as indicated by dense and decreased cycled Zn. This phenomenon further

demonstrates that the cell employed without the OL additive failed because of the Zn dendrite growth and corrosion. The OL additive could boost the uniform nucleation of Zn^{2+} and suppress Zn dendrites, resulting in a uniform electric field of the Zn anode surface.

Schematic illustrations of the Zn plating mechanism are shown in Fig. 4e. The main crystal planes of Zn are (002), (100), and (101), with each of them exhibiting different deposition behaviors. A disordered crystal orientation leads to random growth of Zn. Therefore, zinc dendrites are easily generated and

eventually pierce the separator and cause a short circuit. The presence of OL can regulate the deposition behavior of Zn and guide the epitaxial growth of Zn. A lower angle of 47.6° is characteristic of $Zn(OTF)_2$/OL compared with 71.7° in $Zn(OTF)_2$ (Fig. S17, ESI†). The change in the hydrophilicity demonstrates the enhanced favorable adsorption of OL on the Zn anode, which boosts smooth Zn deposition.[15] The wettability of Zn foil will directly impact the energy barrier for the formation and evolution of Zn nucleation.[48]

Chronoamperometry (CA) has often been used to verify the Zn deposition behavior at a constant voltage of −150 mV (Fig. 4f). In the $Zn(OTF)_2$ electrolyte, Zn exhibits a two-dimensional (2D) diffusion pattern and a huge drop in current density. The continued 2D diffusion is mainly due to the formation of Zn dendrites, corresponding to heterogeneous Zn nucleation.[49] In contrast, the current density is observed to be well maintained in the designed electrolyte. A 3D diffusion process was observed after the 90 s nucleation stage, indicating that the flat and smooth anode surface could be well maintained over the whole 600 s electrochemical process. This result proves that the OL additive relieves side reactions and inhibits the random diffusion behavior of Zn^{2+}. The $Zn(OTF)_2$/OL electrolyte is more favorable for the 3D diffusion of Zn^{2+}.

Furthermore, the nucleation overpotential (NOP) of Zn in the $Zn(OTF)_2$ and $Zn(OTF)_2$/OL electrolytes was further evaluated using Zn‖Cu cells (Fig. 4g). The NOP of Zn increased from 0.164 V in $Zn(OTF)_2$ to 0.415 V when OL was incorporated in 2 m $Zn(OTF)_2$ electrolyte. The higher NOP of Zn, which may be due to the strong solvation of Zn^{2+}, would lead to Zn atoms adsorbing on the Zn anode, facilitating more smooth and uniform Zn deposition with a fine nucleation size.[50,51]

Linear sweep voltammetry (LSV) at a scan rate of 0.5 mV s^{-1} was also performed (Fig. 4h). A narrow electrochemical window and higher corrosion current density were confirmed in $Zn(OTF)_2$. The current response for the $Zn(OTF)_2$/OL electrolyte was initially more negative than that of the $Zn(OTF)_2$ electrolyte, which indicates that the modified electrolyte improves the stability of H_2O. To explore the degree of corrosion of Zn anodes employed in the designed electrolyte, Tafel plots were collected (Fig. S18, ESI†). Compared with the $Zn(OTF)_2$ electrolyte, the Zn anode in the $Zn(OTF)_2$/OL electrolyte showed more positive corrosion potential and lower current density, indicating a reduced tendency toward corrosion reactions and a decreased corrosion rate. These results are well consistent with the spectroscopic results of ^1H NMR, FTIR, and Raman spectroscopy, because the participation of OL destroys the hydrogen bonds of H_2O. Therefore, the side reactions are suppressed.

Electrochemical stability assessment of the Zn anode

To investigate the effect of the OL additive on the stability of the Zn electrode, Zn‖Zn symmetric cells were tested in different modified electrolytes. Among the various electrolytes with different OL ratios, the symmetric cell with 7.5% vol OL addition to its electrolyte showed superior cycling stability to others, cycling for 3200 h at a normal current density of 1 mA cm^{-2} and an areal capacity of 1 mA h cm^{-2} (Fig. S19, ESI†). Thus,

$Zn(OTF)_2$/OL with 7.5 vol% OL was chosen as the representative electrolyte for the other tests, unless otherwise stated. In contrast, the Zn‖Zn symmetric cell with the $Zn(OTF)_2$ electrolyte failed after cycling for 80 h under the same testing conditions, with a sudden polarization voltage fluctuation, as shown in Fig. 5a. The cells based on $Zn(OTF)_2$/OL have a higher average hysteresis voltage, which may be caused by the addition of the OL additive, improving the interfacial desolvation energy barrier. On the other hand, the presence of OL inevitably enlarges the size of the solvated ion complex, and the ion transfer kinetics will decrease accordingly.[52] Therefore, the charge transfer resistance of the $Zn(OTF)_2$/OL electrolyte increases (Fig. S20, ESI†). Even under the harsh conditions of 5 mA cm^{-2} and 5 mA h cm^{-2} (Fig. 5b and S21, ESI†), the Zn electrode with the optimized electrolyte retains a long cycling life above 520 h, further proving that OL plays a significant role in uniform Zn stripping and plating. In contrast, the Zn electrode in $Zn(OTF)_2$ shows a short circuit within 20 h. These results indicate that the OL additive boosts the stability and reversibility of the Zn anode. The rate performance of Zn‖Zn cells was also studied at various current densities and areal capacities (Fig. 5c and S22, ESI†). The cell with the $Zn(OTF)_2$/OL electrolyte shows a more stable voltage profile than that with $Zn(OTF)_2$, even as the current density and capacity increase from 1 mA cm^{-2} and 1 mA h cm^{-2} to 10 mA cm^{-2} and 10 mA h cm^{-2}. To investigate the dendrite suppression mechanism, the kinetics of Zn deposition in different electrolytes were evaluated. According to the rate performance of symmetric cells in different electrolytes, the exchange current density can be calculated (Fig. S23, ESI†). The deposition in the $Zn(OTF)_2$/OL electrolyte shows a lower exchange current density of 21.83 mA cm^{-2}. It is generally believed that the rate of dendrite growth is closely linked to the kinetics of zinc electrodeposition. Reducing the exchange current density can improve the effectiveness of dendrite inhibition.[53]

This remarkable cyclability under different test settings is outstanding compared to previously published studies on the design of the electrolyte for aqueous zinc metal batteries (AZMBs, Fig. 5d and Table S1, ESI†). [32,41,54–62] The asymmetric Zn‖Cu cells were then used to investigate the reversibility of Zn plating and stripping. The CE curve of the Zn‖Cu cell with $Zn(OTF)_2$ was unstable and failed quickly in the 80th cycle (Fig. 5e). In the sharp contrast, the cell that was cycled in $Zn(OTF)_2$/OL was stable up to 1400 cycles with a high average CE of 99.3%. Additionally, the designed electrolyte provided stable voltage profiles and capacity during the Zn plating/stripping process (Fig. 5f and g), where the overpotential was still stable after 500 cycles. Meanwhile, the Zn‖Cu cell in $Zn(OTF)_2$ displayed fluctuating capacity. The plating/stripping voltage profiles of the Zn‖Cu cell with the $Zn(OTF)_2$ electrolyte display fluctuations and the cell failed quickly after 115 cycles (Fig. S24, ESI†). In contrast, a stable performance is achieved for the Zn‖Cu cell with the $Zn(OTF)_2$/OL electrolyte, illustrating a highly reversible plating/stripping process enabled by the OL additive. Meanwhile, the voltage hysteresis measured after the 1000th cycle is only 89 mV. These results illustrate the highly reversible nature of the Zn plating/stripping process in
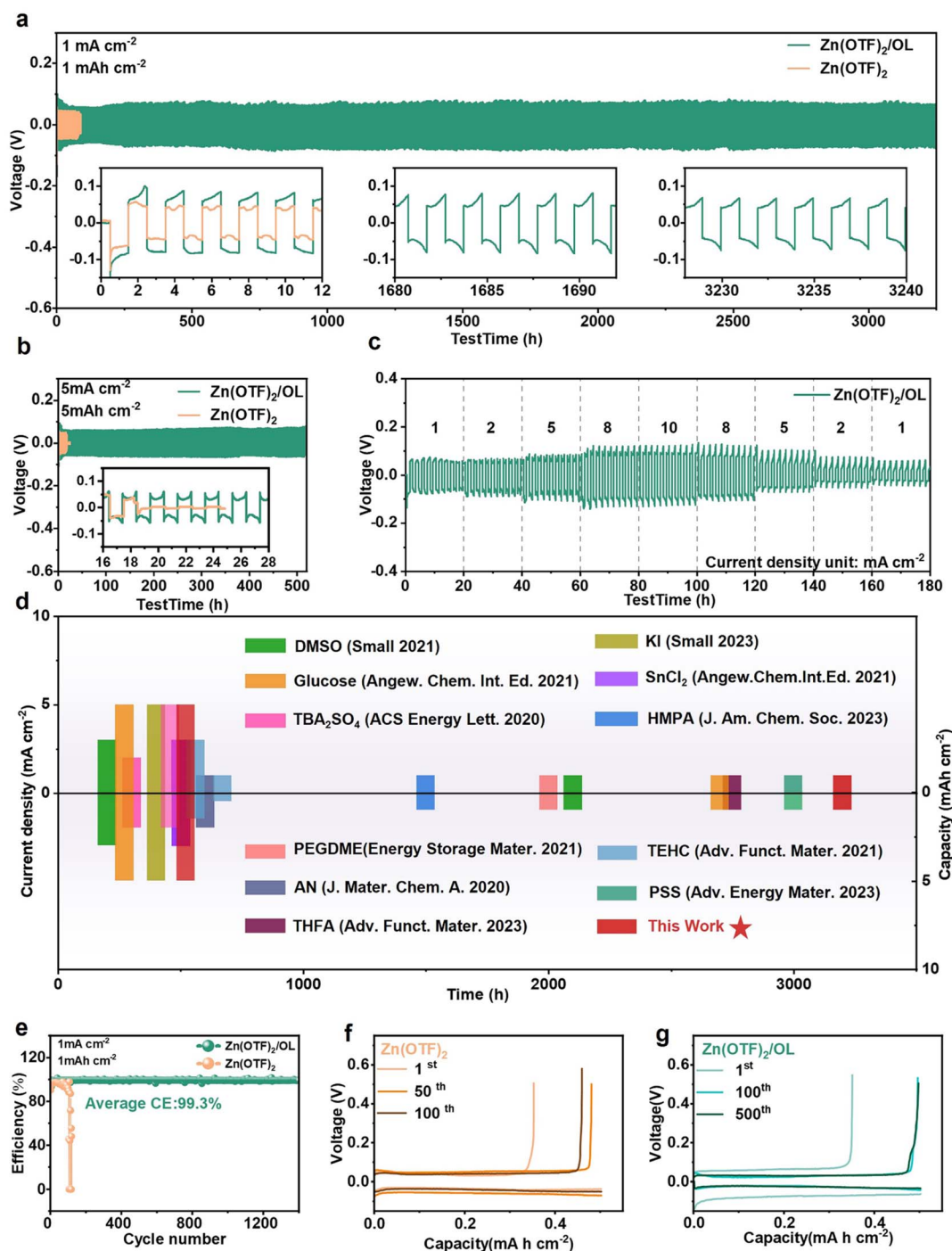
Fig. 5 Electrochemical performance of Zn electrodes. Long-term cycling performance comparison of Zn–Zn symmetric cells at current densities and areal capacities of (a) 1 mA cm^{-2} and 1 mA h cm^{-2}, and (b) 5 mA cm^{-2} and 5 mA h cm^{-2} in different electrolytes. (c) The rate performance of the Zn symmetric cell using the Zn(OTF)$_2$/OL electrolyte. (d) Comparison of cyclic reversibility between this work and other previous reports. (e) Coulombic efficiency of Zn plating/stripping on Cu in Zn(OTF)$_2$/OL and Zn(OTF)$_2$ at 1 mA cm^{-2} and 1 mA h cm^{-2}. Corresponding voltage profiles of the Zn‖Cu cells in (f) Zn(OTF)$_2$ and (g) Zn(OTF)$_2$/OL in different cycles.

Zn(OTF)$_2$/OL, which dramatically improved the stability of the Zn‖Cu cell. Such excellent electrochemical performance demonstrates that the OL additive could not only facilitate the uniform stripping of Zn, but also restrained the side reactions at the interphase between the anode and the electrolyte, and consequently improved the Zn utilization.

Electrochemical performance of the Zn‖NVO full cell

To further verify the practical utility of the OL additive, full cells with Zn(OTF)$_2$ and Zn(OTF)$_2$/OL electrolytes were fabricated using NaV$_3$O$_8$·1.5 H$_2$O (NVO) as the cathode material (Fig. 6a). Based on a previous publication, NVO nanobelts were prepared, and their crystalline phase and morphology were confirmed
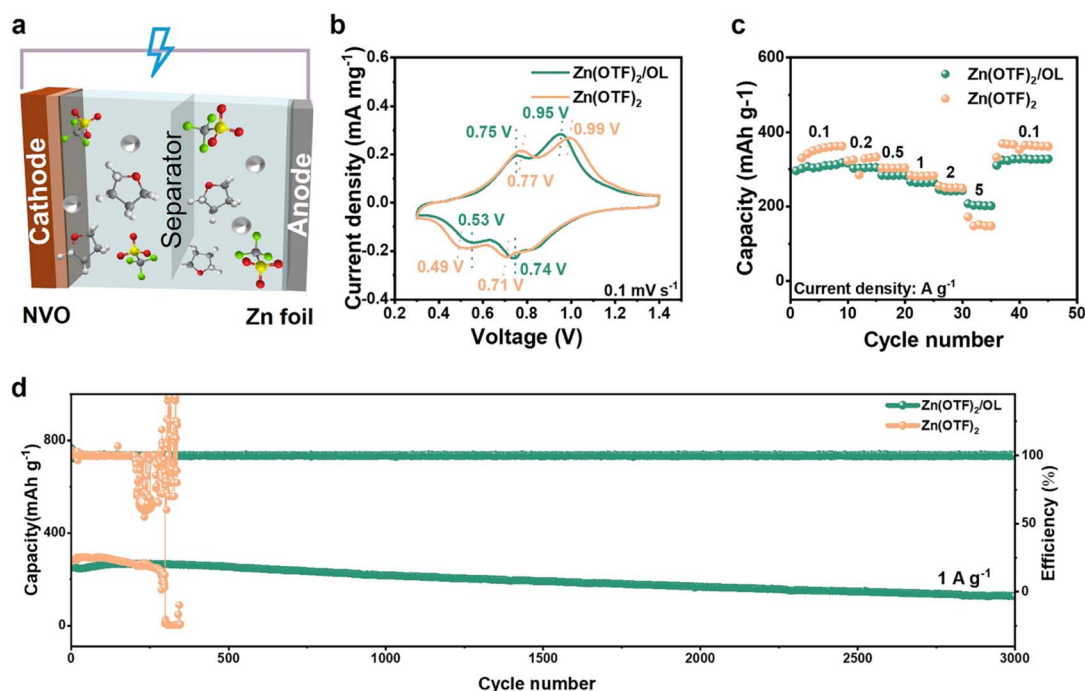
Fig. 6 Electrochemical performance of Zn‖NVO full cells using different electrolytes. (a) Schematic illustration showing the working process of full cells with the OL additives. (b) Cyclic voltammetry curves for the 1st cycle. (c) Rate capability at 0.1, 0.2, 0.5, 1, 2, and 5 A g^{-1} and back to 0.1 A g^{-1}. (d) Cycling performance of full cells with different electrolytes.

(Fig. S25 and S26, ESI†).[63] The cyclic voltammetry (CV) curves of the first cycle for the Zn‖NVO full cell with different electrolytes are shown in Fig. 6b, where both CV curves show two redox peaks and similar behavior (0.53/0.75 V and 0.74/0.95 V), demonstrating that OL did not alter the redox reactions of NVO. The cell that employed the Zn(OTF)$_2$/OL electrolyte displayed higher current density and more obvious polarization in comparison with that in the Zn(OTF)$_2$ electrolyte. Fig. 6c and S27 (ESI)† show the rate capability of the Zn‖NVO full cell with and without OL at various current densities from 0.1 to 5 A g^{-1}. The rate results show that the Zn‖NVO full cells delivered similar capacities at low current density with Zn(OTF)$_2$ and Zn(OTF)$_2$/OL electrolytes. It is clear, however, that the optimized electrolyte exhibits better rate performance at high current densities. With the addition of OL, the capacity of the cell was 207 mA h g^{-1} at 5 A g^{-1}. In contrast, the capacity of the cell with the pure electrolyte was only 142 mA h g^{-1} at 5 A g^{-1}. The long-term cycling stability (Fig. 6d) of the Zn‖NVO full cells with both electrolytes was investigated at 1 A g^{-1}. Benefiting from the improved stability of the Zn anode in the OL-containing electrolyte, the full cells exhibited excellent cycling stability in the Zn(OTF)$_2$/OL electrolyte. After the initial 3 cycles tested at 0.1 A g^{-1}, the cell achieved a high capacity of 248.9 mA h g^{-1} and exhibited a slight decline until 3000 cycles. To investigate the cyclability of full cells, the capacity retention is directly measured. The capacity retention can reach 78.8% when the full cells exhibit excellent cycling stability in Zn(OTF)$_2$/OL after 3000 cycles at 1 A g^{-1}. In contrast, the Zn‖NVO full cell without OL showed rapid decay and a short circuit after 500 cycles.

Moreover, Zn‖NVO full cells with both electrolytes were investigated at 0.2 A g^{-1} (Fig. S28, ESI†). The capacity stability of zinc-ion batteries at low current densities is essential for a range of practical applications. The cell with the Zn(OTF)$_2$/OL electrolyte exhibits cycling stability, achieving 170 cycles (still in progress in the lab) and starting with a high specific discharge capacity of 210 mA h g^{-1}. In comparison, the cell with the Zn(OTF)$_2$ electrolyte is unstable after 110 cycles. In addition, the long-term cycling performance of the full cells at a larger current density of 5 A g^{-1} was tested (Fig. S29, ESI†). The full cell with the Zn(OTF)$_2$/OL electrolyte can deliver a high discharge capacity (237.5 mA h g^{-1}) after 1400 cycles, and the capacity retention is 89.9%. Obviously, the cyclability can be improved with the addition of OL. The cell with the Zn(OTF)$_2$ electrolyte experienced a short circuit after 340 cycles. The full cell result shows great potential for application of the Zn(OTF)$_2$/OL electrolyte.

According to the above experimental and theoretical results, the overall mechanism of OL for boosting Zn tip dissolution and suppressing Zn dendrites can be summarized in Fig. 7. In the traditional Zn(OTF)$_2$ electrolyte, Zn dissolves unevenly. The non-uniform stripping of Zn leads to the formation of hollows on the Zn anode. Additionally, side reactions, including corrosion reactions and the hydrogen evolution reaction (HER), can lead to the formation of by-products on the Zn anode. Furthermore, the free diffusion of Zn^{2+} leads to serious dendrite growth. All these situations result in poor electrochemical performance. In striking contrast, after adding OL, the OL molecules gather at the Zn tips, thus facilitating the loss of electrons from Zn metal atoms to transform them into Zn^{2+} and
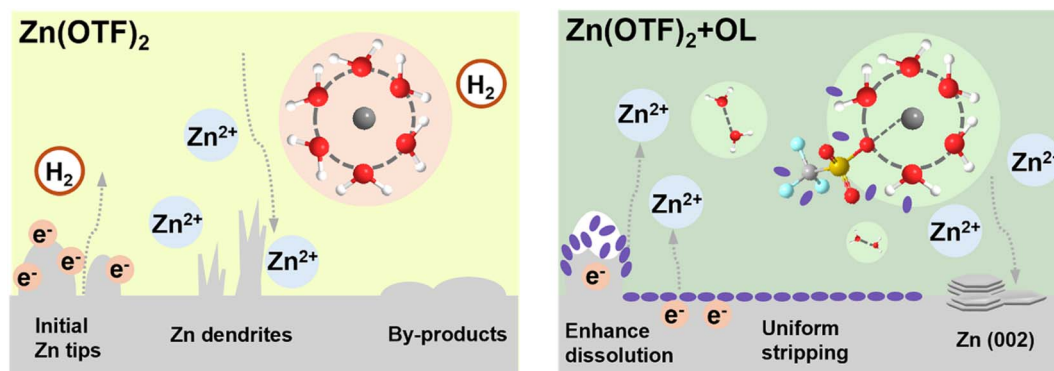
Fig. 7 Schematic illustrations of the stripping mechanism in Zn (OTF)$_2$ and the stripping-modulation mechanism in Zn (OTF)$_2$/OL.

thereby regulating uniform stripping. The preferred Zn (002) restrains the formation of dendrites.

Conclusions

In this work, we have demonstrated an electron-loss regulation strategy for stripping modulation that enables superior performance of Zn anodes. OL was used as a model additive to promote electron loss from Zn metal and induce oriented Zn deposition. During Zn stripping, OL adsorbs on and concentrates at the tips of the Zn surface, boosting the dissolving speed of the initial protuberant tips, which consequently leads to uniform stripping. As for plating, experimental characterization and theoretical simulations confirmed that OL molecules induce the (002) orientation for Zn deposition, which tends to inhibit dendrite growth. Therefore, the growth of zinc dendrites is inhibited. The OL additive reduces the activity of H$_2$O and optimizes the solvation structure of Zn^{2+}. Our designed electrolyte promoted a longer cycling lifespan for our symmetrical Zn‖Zn cells over 3200 h at 1 mA cm^{-2} and 1 mA h cm^{-2}. Their much higher CE (99.3%) at 1 mA cm^{-2} and 1 mA h cm^{-2} for more than up to 1400 cycles also indicated the potential of OL. Therefore, this strategy provides a new direction for the development of stable Zn anodes and the possibility of high-performance commercial AZIBs.

Data availability

The data supporting this article have been included as part of the ESI.†

Author contributions

X. W. and L. L. contributed equally to this work. X. W., L. L., and W. L. conceptualized the idea and designed the experiments. X. W. conducted the experiments and the data analysis. L. L. and Z. H. assisted in the materials characterization. L. L. performed theoretical calculations. X. W. wrote the original draft. C. H., X. X., S. X. D., and W. L. reviewed and revised the manuscript. All authors discussed the results and approved the submission.

Conflicts of interest

The authors declare no competing financial interests.

Acknowledgements

References

1 G. Li, Z. Zhao, S. Zhang, L. Sun, M. Li, J. A. Yuwono, J. Mao, J. Hao, J. Vongsvivut, L. Xing, C.-X. Zhao and Z. Guo, A biocompatible electrolyte enables highly reversible Zn anode for zinc ion battery, *Nat. Commun.*, 2023, **14**, 6526.

2 J. Dong, L. Su, H. Peng, D. Wang, H. Zong, G. Wang and J. Yang, Spontaneous Molecule Aggregation for Nearly Single-Ion Conducting Sol Electrolyte to Advanced Aqueous Zinc Metal Batteries: The Case of Tetraphenylporphyrin, *Angew. Chem., Int. Ed.*, 2024, e202401441.

3 Z. Zhang, P. Wang, C. Wei, J. Feng, S. Xiong and B. Xi, Synchronous Regulation of d-Band Centers in Zn Substrates and Weakening Pauli Repulsion of Zn ions using the Ascorbic Acid Additive for Reversible Zinc Anodes, *Angew. Chem.*, 2024, e202402069.

4 L. Liu, H. Lu, C. Han, X. Chen, S. Liu, J. Zhang, X. Chen, X. Wang, R. Wang, J. Xu, H. K. Liu, S. X. Dou and W. Li, Salt Anion Amphiphilicity-Activated Electrolyte Cosolvent Selection Strategy toward Durable Zn Metal Anode, *ACS Nano*, 2023, **17**, 23065–23078.

5 X. Wang, C. Han, S. Dou and W. Li, The protective effect and its mechanism for electrolyte additives on the anode interface in aqueous zinc-based energy storage devices, *Nano Mater. Sci.*, 2022, DOI: 10.1016/j.nanoms.2022.10.004.

6 W. Li, C. Han, Q. Gu, S. L. Chou, J. Z. Wang, H. K. Liu and S. X. Dou, Electron Delocalization and Dissolution-Restraint in Vanadium Oxide Superlattices to Boost Electrochemical Performance of Aqueous Zinc-Ion Batteries, *Adv. Energy Mater.*, 2020, **10**, 2001852.

7 X. Wang, L. Liu, Z. Hu, C. Peng, C. Han and W. Li, High Energy Density Aqueous Zinc–Chalcogen (S, Se, Te) Batteries: Recent Progress, Challenges, and Perspective, *Adv. Energy Mater.*, 2023, **13**, 2302927.

8 J. Abdulla, J. Cao, P. Wangyao and J. Qin, Review on the suppression of Zn dendrite for high performance of Zn ion battery, *J. Met., Mater. Miner.*, 2020, **30**.

9 Q. Zheng, Z. Hu, L. Liu, H. Lu, X. Wang, Y. Lei, C. Han and W. Li, Recent advances and perspectives of 1D/2D carbon materials for high-performance flexible zinc ion batteries, *J. Mater. Chem. A*, 2024, **12**, 21531–21552.

10 Q. Zhang, J. Luan, X. Huang, Q. Wang, D. Sun, Y. Tang, X. Ji and H. Wang, Revealing the role of crystal orientation of protective layers for stable zinc anode, *Nat. Commun.*, 2020, **11**, 1–7.

11 H. Qiu, X. Du, J. Zhao, Y. Wang, J. Ju, Z. Chen, Z. Hu, D. Yan, X. Zhou and G. Cui, Zinc anode-compatible *in situ* solid electrolyte interphase *via* cation solvation modulation, *Nat. Commun.*, 2019, **10**, 5374.

12 J. Shin, J. Lee, Y. Park and J. W. Choi, Aqueous zinc ion batteries: focus on zinc metal anodes, *Chem. Sci.*, 2020, **11**, 2028–2044.

13 C. Yang, P. Woottapanit, Y. Yue, S. Geng, J. Cao, X. Zhang, G. He and J. Qin, Industrial Waste Derived Separators for Zn-Ion Batteries Achieve Homogeneous Zn (002) Deposition Through Low Chemical Affinity Effects, *Small*, 2024, 2311203.

14 P. Chen, X. Yuan, Y. Xia, Y. Zhang, L. Fu, L. Liu, N. Yu, Q. Huang, B. Wang and X. Hu, An Artificial Polyacrylonitrile Coating Layer Confining Zinc Dendrite Growth for Highly Reversible Aqueous Zinc-Based Batteries, *Advanced Science*, 2021, 2100309.

15 C. Deng, X. Xie, J. Han, Y. Tang, J. Gao, C. Liu, X. Shi, J. Zhou and S. Liang, A sieve-functional and uniform-porous kaolin layer toward stable zinc metal anode, *Adv. Funct. Mater.*, 2020, **30**, 2000599.

16 L. Zhuo, T. T. BEYENE, Z. Kai and C. Dianxue, Realizing fast plating/stripping of high-performance Zn metal anode with a low Zn loading, *J. Met., Mater. Miner.*, 2024, **34**, 2009.

17 L. Cao, D. Li, E. Hu, J. Xu, T. Deng, L. Ma, Y. Wang, X.-Q. Yang and C. Wang, Solvation structure design for aqueous Zn metal batteries, *J. Am. Chem. Soc.*, 2020, **142**, 21404–21409.

18 J. Cong, X. Shen, Z. Wen, X. Wang, L. Peng, J. Zeng and J. Zhao, Ultra-stable and highly reversible aqueous zinc metal anodes with high preferred orientation deposition achieved by a polyanionic hydrogel electrolyte, *Energy Storage Mater.*, 2021, **35**, 586–594.

19 L. Liu, X.-Y. Wang, Z. Hu, X. Wang, Q. Zheng, C. Han, J. Xu, X. Xu, H.-K. Liu and S.-X. Dou, Electric Double Layer Regulator Design through a Functional Group Assembly Strategy towards Long-lasting Zinc Metal Batteries, *Angew. Chem.*, 2024, e202405209.

20 J. Cao, M. Sun, D. Zhang, Y. Zhang, C. Yang, D. Luo, X. Yang, X. Zhang, J. Qin, B. Huang, Z. Zeng and J. Lu, Tuning Vertical Electrodeposition for Dendrites-Free Zinc-Ion Batteries, *ACS Nano*, 2024, **18**, 16610–16621.

21 D. Zhang, J. Cao, Z. Dai, R. Chanajaree, C. Yang, X. Wu, X. Zhang and J. Qin, A long-term stable zinc metal anode enabled by a mannitol additive, *J. Mater. Chem. A*, 2023, **11**, 23779–23786.

22 Y. Zeng, X. Zhang, R. Qin, X. Liu, P. Fang, D. Zheng, Y. Tong and X. Lu, Dendrite-Free Zinc Deposition Induced by Multifunctional CNT Frameworks for Stable Flexible Zn-Ion Batteries, *Adv. Mater.*, 2019, **31**, 1903675.

23 Q. Li, Y. Wang, F. Mo, D. Wang, G. Liang, Y. Zhao, Q. Yang, Z. Huang and C. Zhi, Calendar Life of Zn Batteries Based on Zn Anode with Zn Powder/Current Collector Structure, *Adv. Energy Mater.*, 2021, **11**, 2003931.

24 J. Cao, X. Wang, D. Zhang, D. Luo, L. Zhang, J. Qin, X. Zhang and X. Yang, Pre-Corrosion of Zinc Metal Anodes for Enhanced Stability and Kinetics, *Small*, 2024, 2403622.

25 S. Guo, L. Qin, T. Zhang, M. Zhou, J. Zhou, G. Fang and S. Liang, Fundamentals and perspectives of electrolyte additives for aqueous zinc-ion batteries, *Energy Storage Mater.*, 2020, 545–562.

26 N. Chang, T. Li, R. Li, S. Wang, Y. Yin, H. Zhang and X. Li, An aqueous hybrid electrolyte for low-temperature zinc-based energy storage devices, *Energy Environ. Sci.*, 2020, **13**, 3527–3535.

27 X. Guo, Z. Zhang, J. Li, N. Luo, G.-L. Chai, T. S. Miller, F. Lai, P. Shearing, D. J. Brett and D. Han, Alleviation of Dendrite Formation on Zinc Anodes *Via* Electrolyte Additives, *ACS Energy Lett.*, 2021, **6**, 395–403.

28 W. Xu, K. Zhao, W. Huo, Y. Wang, G. Yao, X. Gu, H. Cheng, L. Mai, C. Hu and X. Wang, Diethyl ether as self-healing electrolyte additive enabled long-life rechargeable aqueous zinc ion batteries, *Nano Energy*, 2019, **62**, 275–281.

29 D. Yuan, J. Zhao, H. Ren, Y. Chen, R. Chua, E. T. J. Jie, Y. Cai, E. Edison, W. Manalastas Jr and M. W. Wong, Anion texturing towards dendrite-free Zn anode for aqueous rechargeable batteries, *Angew. Chem.*, 2021, **133**, 7289–7295.

30 M. Qiu, P. Sun, A. Qin, G. Cui and W. Mai, Metal-coordination chemistry guiding preferred crystallographic orientation for reversible zinc anode, *Energy Storage Mater.*, 2022, **49**, 463–470.

31 D. Li, L. Cao, T. Deng, S. Liu and C. Wang, Design of a Solid Electrolyte Interphase for Aqueous Zn Batteries, *Angew. Chem., Int. Ed.*, 2021, **60**, 13035–13041.

32 L. Cao, D. Li, F. A. Soto, V. Ponce, B. Zhang, L. Ma, T. Deng, J. M. Seminario, E. Hu and X. Q. Yang, Highly Reversible Aqueous Zinc Batteries enabled by Zincophilic–Zincophobic Interfacial Layers and Interrupted Hydrogen-Bond Electrolytes, *Angew. Chem., Int. Ed.*, 2021, **60**, 18845–18851.

33 H. Jia, Z. Wang, B. Tawiah, Y. Wang, C.-Y. Chan, B. Fei and F. Pan, Recent advances in zinc anodes for high-performance aqueous Zn-ion batteries, *Nano Energy*, 2020, **70**, 104523.

34 C. Li, Z. Sun, T. Yang, L. Yu, N. Wei, Z. Tian, J. Cai, J. Lv, Y. Shao and M. H. Rümmeli, Directly grown vertical graphene carpets as janus separators toward stabilized Zn metal anodes, *Adv. Mater.*, 2020, **32**, 2003425.

35 R. Zhao, Y. Yang, G. Liu, R. Zhu, J. Huang, Z. Chen, Z. Gao, X. Chen and L. Qie, Redirected Zn electrodeposition by an anti-corrosion elastic constraint for highly reversible Zn anodes, *Adv. Funct. Mater.*, 2021, **31**, 2001867.

36 Q. Li, A. Chen, D. Wang, Y. Zhao, X. Wang, X. Jin, B. Xiong and C. Zhi, Tailoring the metal electrode morphology *via* electrochemical protocol optimization for long-lasting aqueous zinc batteries, *Nat. Commun.*, 2022, **13**, 3699.

37 H. Ji, Z. Han, Z. Lin, B. Yu, D. Wu, L. Zhao, M. Wang, J. Chen, Z. Ma, B. Guo, Y. Huang and X. Li, Stabilizing zinc anode for high-performance aqueous zinc ion batteries *via* employing a novel inositol additive, *J. Alloys Compd.*, 2022, **914**, 165231.

38 V. Gutmann, *The donor–acceptor approach to molecular interactions*, Springer, 1978.

39 J. W. Kim and A. Kim, Absolute work function measurement by using photoelectron spectroscopy, *Curr. Appl. Phys.*, 2021, **31**, 52–59.

40 D. D. Purkayastha and V. Madhurima, Interactions in water–THF binary mixture by contact angle, FTIR and dielectric studies, *J. Mol. Liq.*, 2013, **187**, 54–57.

41 P. Sun, L. Ma, W. Zhou, M. Qiu, Z. Wang, D. Chao and W. Mai, Simultaneous regulation on solvation shell and electrode interface for dendrite-free Zn ion batteries achieved by a low-cost glucose additive, *Angew. Chem.*, 2021, **133**, 18395–18403.

42 G. Liang, Z. Tang, B. Han, J. Zhu, A. Chen, Q. Li, Z. Chen, Z. Huang, X. Li, Q. Yang and C. Zhi, Regulating Inorganic and Organic Components to Build Amorphous-ZnFx Enriched Solid-Electrolyte Interphase for Highly Reversible Zn Metal Chemistry, *Adv. Mater.*, 2023, 2210051.

43 S. Liu, J. Mao, W. K. Pang, J. Vongsvivut, X. Zeng, L. Thomsen, Y. Wang, J. Liu, D. Li and Z. Guo, Tuning the Electrolyte Solvation Structure to Suppress Cathode Dissolution, Water Reactivity, and Zn Dendrite Growth in Zinc-Ion Batteries, *Adv. Funct. Mater.*, 2021, **31**, 2104281.

44 G. Ma, L. Miao, Y. Dong, W. Yuan, X. Nie, S. Di, Y. Wang, L. Wang and N. Zhang, Reshaping the electrolyte structure and interface chemistry for stable aqueous zinc batteries, *Energy Storage Mater.*, 2022, **47**, 203.

45 M. Zhou, S. Guo, J. Li, X. Luo, Z. Liu, T. Zhang, X. Cao, M. Long, B. Lu and A. Pan, Surface-Preferred Crystal Plane for a Stable and Reversible Zinc Anode, *Adv. Mater.*, 2021, **33**, 2100187.

46 X. Jia, C. Liu, Z. G. Neale, J. Yang and G. Cao, Active materials for aqueous zinc ion batteries: synthesis, crystal structure, morphology, and electrochemistry, *Chem. Rev.*, 2020, **120**, 7795–7866.

47 S. Wang, G. Liu and L. Wang, Crystal Facet Engineering of Photoelectrodes for Photoelectrochemical Water Splitting, *Chem. Rev.*, 2019, **119**, 5192–5247.

48 J. Hao, L. Yuan, C. Ye, D. Chao, K. Davey, Z. Guo and S. Z. Qiao, Boosting Zinc Electrode Reversibility in Aqueous Electrolytes by Using Low-Cost Antisolvents, *Angew. Chem.*, 2021, **133**, 7442–7451.

49 H. Yang, Y. Qiao, Z. Chang, H. Deng, X. Zhu, R. Zhu, Z. Xiong, P. He and H. Zhou, Reducing Water Activity by Zeolite Molecular Sieve Membrane for Long-Life Rechargeable Zinc Battery, *Adv. Mater.*, 2021, **33**, 2102415.

50 A. Pei, G. Zheng, F. Shi, Y. Li and Y. Cui, Nanoscale nucleation and growth of electrodeposited lithium metal, *Nano Lett.*, 2017, **17**, 1132–1139.

51 Z. Zhao, J. Zhao, Z. Hu, J. Li, J. Li, Y. Zhang, C. Wang and G. Cui, Long-life and deeply rechargeable aqueous Zn anodes enabled by a multifunctional brightener-inspired interphase, *Energy Environ. Sci.*, 2019, **12**, 1938–1949.

52 J. Z. Hu, N. R. Jaegers, N. T. Hahn, W. Hu, K. S. Han, Y. Chen, J. A. Sears, V. Murugesan, K. R. Zavadil and K. T. Mueller, Understanding the Solvation-Dependent Properties of Cyclic Ether Multivalent Electrolytes Using High-Field NMR and Quantum Chemistry, *JACS Au*, 2022, **2**, 917–932.

53 M. Luo, C. Wang, H. Lu, Y. Lu, B. B. Xu, W. Sun, H. Pan, M. Yan and Y. Jiang, Dendrite-free zinc anode enabled by zinc-chelating chemistry, *Energy Storage Mater.*, 2021, **41**, 515–521.

54 Y. Wu, T. Zhang, L. Chen, Z. Zhu, L. Cheng, S. Gu, Z. Li, Z. Tong, H. Li, Y. Li, Z. Lu, W. Zhang and C. S. Lee, Polymer Chain-Guided Ion Transport in Aqueous Electrolytes of Zn-Ion Batteries, *Adv. Energy Mater.*, 2023, **13**, 2300719.

55 S. Wang, Y. Zhao, H. Lv, X. Hu, J. He, C. Zhi and H. Li, Low-Concentration Redox-Electrolytes for High-Rate and Long-Life Zinc Metal Batteries, *Small*, 2023, 2207664.

56 D. Feng, F. Cao, L. Hou, T. Li, Y. Jiao and P. Wu, Immunizing Aqueous Zn Batteries against Dendrite Formation and Side Reactions at Various Temperatures *via* Electrolyte Additives, *Small*, 2021, 2103195.

57 Z. Hou, Z. Lu, Q. Chen and B. Zhang, Realizing wide-temperature Zn metal anodes through concurrent interface stability regulation and solvation structure modulation, *Energy Storage Mater.*, 2021, 517–525.

58 Z. Hou, H. Tan, Y. Gao, M. Li, Z. Lu and B. Zhang, Tailoring desolvation kinetics enables stable zinc metal anodes, *J. Mater. Chem. A*, 2020, **8**, 19367–19374.

59 Y. Qiu, X. Zheng, R. Zhang, Q. Lin, M. Li, J. Luo, S. Yang, Z. Liu, Q. Wang, Y. Yu and C. Yang, Boosting Zinc-Ion Batteries with Innovative Ternary Electrolyte for Enhanced Interfacial Electrochemistry and Temperature-Resilient Performance, *Adv. Funct. Mater.*, 2024, 2310825.

60 A. Bayaguud, X. Luo, Y. Fu and C. Zhu, Cationic surfactant-type electrolyte additive enables three-dimensional dendrite-free zinc anode for stable zinc-ion batteries, *ACS Energy Lett.*, 2020, **5**, 3012–3020.

61 L. Qian, W. Yao, R. Yao, Y. Sui, H. Zhu, F. Wang, J. Zhao, C. Zhi and C. Yang, Cations Coordination-Regulated Reversibility Enhancement for Aqueous Zn-Ion Battery, *Adv. Funct. Mater.*, 2021, **31**, 2105736.

62 M. Kim, J. Lee, Y. Kim, Y. Park, H. Kim and J. W. Choi, Surface Overpotential as a Key Metric for the Discharge–Charge Reversibility of Aqueous Zinc-Ion Batteries, *J. Am. Chem. Soc.*, 2023, **145**, 15776–15787.

63 F. Wan, L. Zhang, X. Dai, X. Wang, Z. Niu and J. Chen, Aqueous rechargeable zinc/sodium vanadate batteries with enhanced performance from simultaneous insertion of dual carriers, *Nat. Commun.*, 2018, **9**, 1–11.